Journal of Materials Science & Technology 37 (2020) 185–199

Contents lists available at ScienceDirect

Journal of Materials Science & Technology

journal homepage: www.jmst.org

Research Article

Graphene oxide effects on the properties of Al_2O_3-Cu/35W5Cr composite

Xiaohui Zhang[a,b,c], Yi Zhang[a,b,c,*], Baohong Tian[a,b,c,*], Yanlin Jia[d,**], Ming Fu[e], Yong Liu[a,b,c], Kexing Song[a,b,c], Alex. A. Volinsky[f], Xiao Yang[g], Hang Sun[a,b,c]

[a] School of Materials Science and Engineering, Henan University of Science and Technology, Luoyang 471023, China
[b] Collaborative Innovation Center of Nonferrous Metals, Henan Province, Luoyang 471023, China
[c] Henan Key Laboratory of Nonferrous Materials Science and Processing Technology, Luoyang 471023, China
[d] College of Materials Science and Engineering, Beijing University of Technology, Beijing 100124, China
[e] China Airborne Missile Academy, Luoyang 471023, China
[f] Department of Mechanical Engineering, University of South Florida, Tampa 33620, USA
[g] Luoyang Ship Material Research Institute, Luoyang 471023, China

ARTICLE INFO

Article history:
Received 27 May 2019
Received in revised form 10 July 2019
Accepted 13 July 2019
Available online 29 August 2019

Keywords:
Graphene oxide
Freeze-drying
Electrical contact
In situ formed Cr_3C_2
Tensile strength

ABSTRACT

Graphene oxide (GO) nanosheets were dispersed into premixed powders (Cu-0.4 wt% Al/35W5Cr) by wet grinding and vacuum freeze-drying process. The 0.3 wt% GO/Al_2O_3-Cu/35W5Cr and 0.5 wt%GO/Al_2O_3-Cu/35W5Cr composites, used for electrical contacts, were fabricated by vacuum hot-pressing sintering. The microstructure was analyzed by field emission scanning electron and transmission electron microscopy. In addition, the Raman spectroscopy and X-ray photoelectron spectroscopy were used to investigate the structural changes of GO before and after sintering. The arc erosion behavior was investigated by the JF04C electrical contact testing apparatus. Consequently, the Al_2O_3 nanoparticles were evenly dispersed in the matrix, causing dislocation tangles. GO was converted to reduced graphene oxide after sintering. A group of carbon atoms combined with Cr forming Cr_3C_2 in situ during sintering, which enhanced the interface bonding. Compared with the Al_2O_3-Cu/35W5Cr composite, the tensile strength of the two contact materials containing 0.3 wt% GO and 0.5 wt% GO was increased by 45% and 34%, respectively. Finally, pips and craters were present on the anode and cathode surfaces, respectively. Tungsten has undergone re-sintering during arcing and formed needle-like structures. Compared with Al_2O_3-Cu/35W5Cr, the GO/Al_2O_3-Cu35W5Cr composites have better welding resistance. The final mass transfer direction of the two composites was from the cathode to anode.

1. Introduction

Electrical contact is a pervasive phenomenon between the two conductors, which are transmitting electrical current. Many physical and chemical effects, such as temperature elevation, welding, wear and arc erosion, take place during initiating, maintaining and terminating electrical contacts. Therefore, electrical contacts play a vital role in connecting circuits, transmitting power, and breaking circuits [1–3]. With the rapid development of the power industry and manufacturing, a single kind of material can no longer satisfy the new requirements for superior electrical contacts. One promising strategy is combining the matrix with different dispersed secondary phases, called the combined strengthening process [4–6]. Compared with the secondary phases, solid solution atoms have dramatic scattering effects on the electrons. However, composites can be mechanically strengthened, while maintaining their required electrical conductivity. More specifically, different composite phases can cause the arc to move rapidly on the contact surfaces, making it difficult to form large liquid metal pools, resulting in reduced liquid splashing [7,8].

Copper matrix composites have been considered as promising electrical contact materials because of their high electrical and thermal conductivity, and high-temperature stability. Different kinds of phases play a significant role in the copper matrix composites. Al_2O_3 nano-particles dispersion-reinforced copper matrix compos-

* Corresponding authors at: School of Materials Science and Engineering, Henan University of Science and Technology, Luoyang 471023, China.
** Corresponding author.
E-mail addresses: zhshgu436@163.com (Y. Zhang), bhtian007@163.com (B. Tian), jiayanlin@126.com (Y. Jia).

https://doi.org/10.1016/j.jmst.2019.08.014
1005-0302/

ites prepared by internal oxidation not only have high strength and conductivity, but also high recrystallization temperature and good thermal stability [9–11]. For example, Tian et al. [12] demonstrated that the softening temperature of Cu-0.5 vol% Al_2O_3 prepared by internal oxidation was 800 °C, and the electrical conductivity was 93% IACS. Tungsten has a high melting point, density, dielectric strength, and low thermal expansion coefficient. With the melting and evaporation of copper under arc erosion in the CuW electrical contacts, W particles are gradually aggregated and sintered into needle-like skeletons, which restrict the flow of copper, thereby improving the arc erosion resistance. These needle-like skeleton structures have been distinctly observed in our previous studies [13]. Chromium has a high melting point, hardness and crispness characteristics, small chopping value and strong breaking capacity. Moreover, great affinity to oxygen ensures good vacuum compatibility [14,15]. Taylor's research [16] indicated that the cathode spot moves faster when the surface of CuCr electrical contacts changes from an early arc column to a diffusion arc, thus avoiding the large-scale erosion of the contact surface by the arc. Consequently, CuCr is considered as a promising electrical contact material for the medium voltage. Furthermore, as strong carbide forming elements, Cr and W in contact materials can form carbides with doped carbon atoms, thereby enhancing the strength of the composites due to better interface bonding and high dislocation density at the interface. For instance, Cr_3C_2 is a widely used metal carbide with a high melting point, hardness, good wettability with metals and strong oxidation resistance.

In recent years, graphene and its derivatives, such as graphene oxide (GO) and reduced graphene oxide (RGO), have drawn more attention as promising reinforcement for metal matrix composites [17]. Graphene is a two-dimensional material with only one atomic layer thickness. It has a honeycomb crystal structure consisting of sp^2 hybridized carbon atoms arranged tightly [18]. Tang et al. [19] found that the yield strength and elastic modulus of copper matrix increased by 94% and 6%, respectively, by adding 1 vol.% graphene nanosheets into the copper matrix. Varol et al. [20] observed that the highest conductivity was 78.5% IACS by adding 0.5 wt% graphene into copper matrix composites. Dong et al. [21] prepared graphene-tungsten-copper composites by the infiltration method. The W particles were refined, and the arc erosion resistance was improved. However, owing to the weak affinity and interfacial bonding between graphene and copper matrix, these issues have restricted its application. However, graphene oxide has a large number of hydrophilic functional groups, such as hydroxyl, epoxy and carboxyl groups, which cause graphene oxide to have good wettability, dispersibility and surface activity. The interface

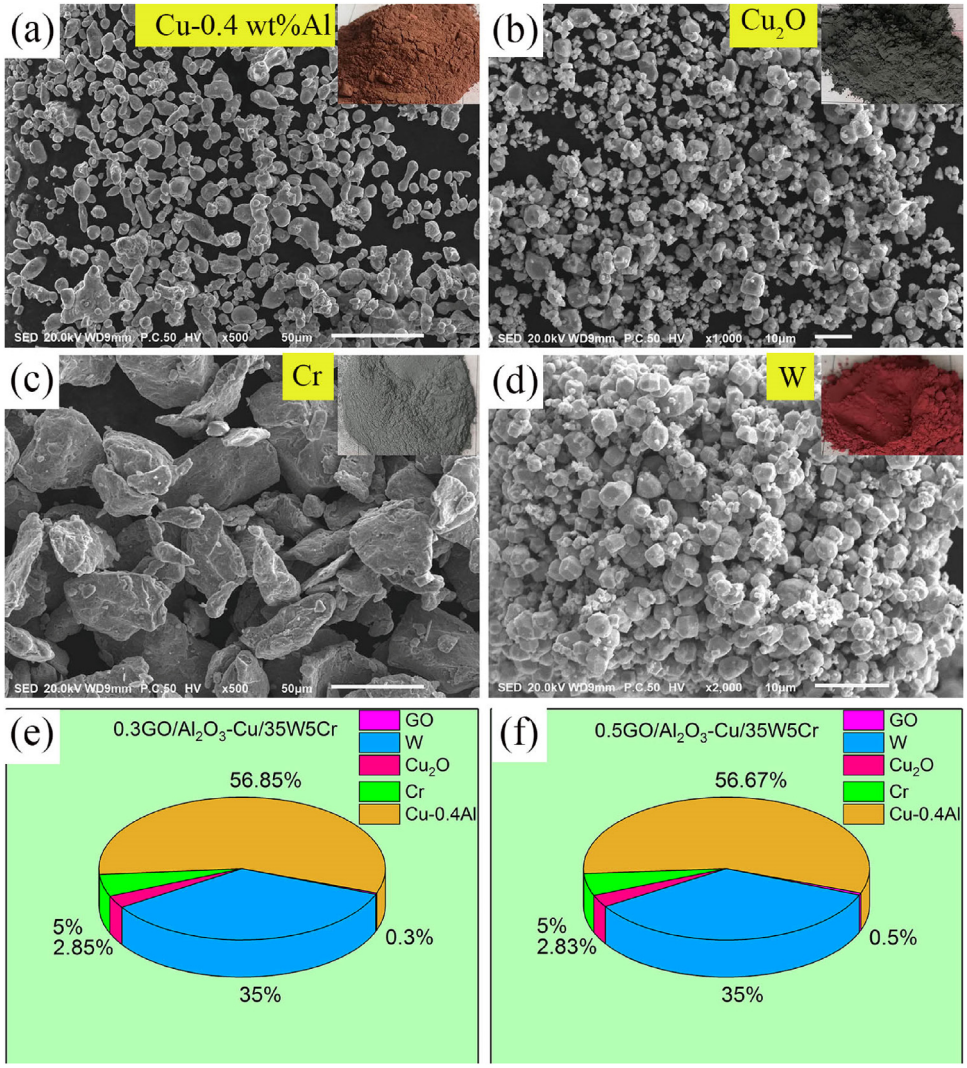

Fig. 1. SEM images of powders and composition ratio: (a) Cu-0.4 wt% Al powder; (b) Cu_2O powder; (c) Cr powder; (d) W powder; (e) composition ratio of 0.3GO/Al_2O_3-Cu/35W5Cr composite; (f) composition ratio of 0.5GO/Al_2O_3-Cu/35W5Cr composite.

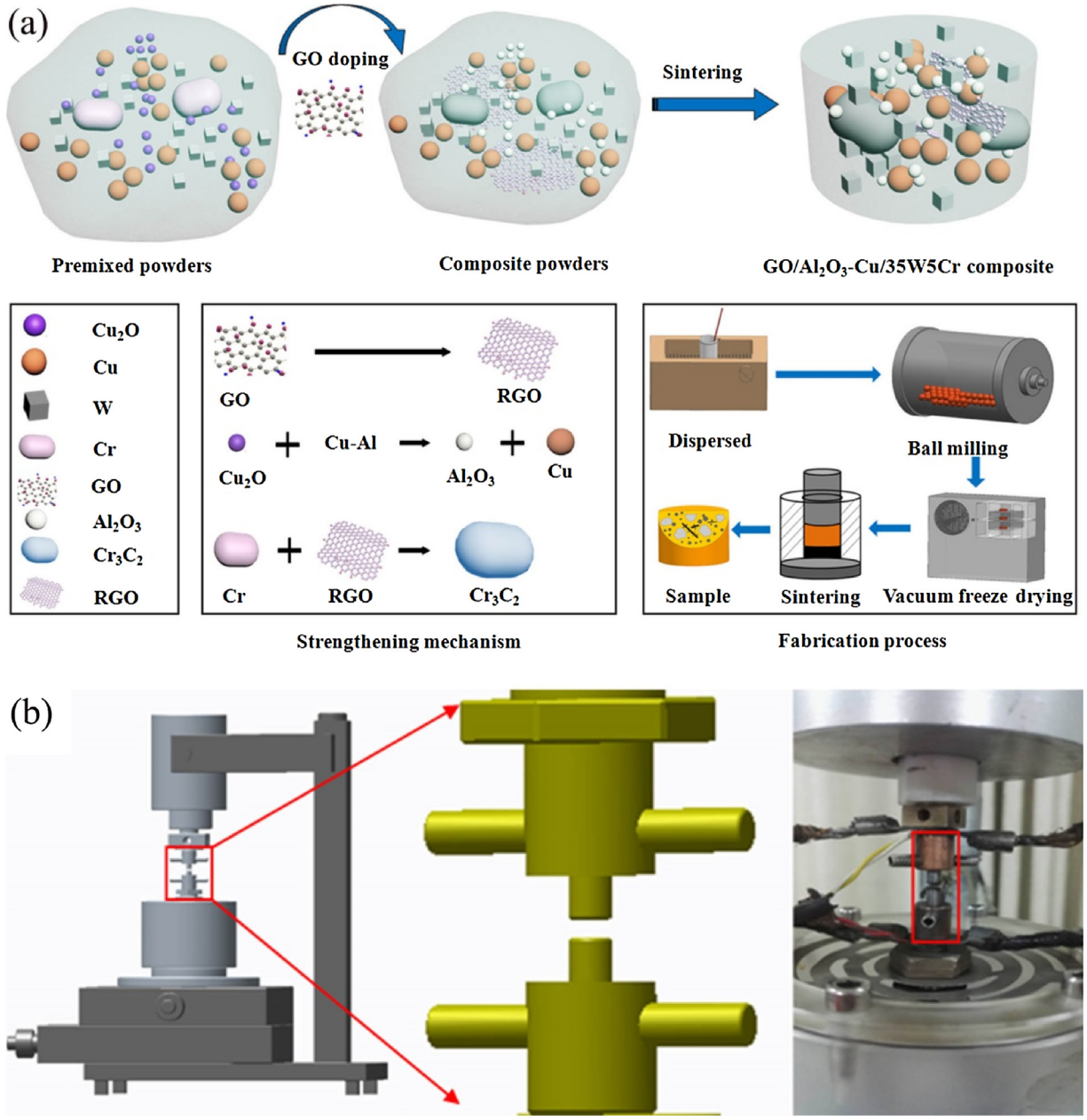

Fig. 2. (a) Schematics of the fabrication process of the composites and (b) electrical contact testing apparatus.

bonding can be optimized to improve the properties of the composites [22,23]. Nevertheless, the excellent electrical and thermal conductivity of graphene is considerably reduced by the functional groups. High conductivity can only be obtained through reduction. The electrical conductivity of GO can be improved by heating to about 900–1000 °C. Because of the loss of functional groups, GO is converted into reduced GO [24,25]. Ramirez et al. [26] observed that GO can be reduced when graphene oxide-doped Si_3N_4 composites were spark plasma sintered. Xia et al. [27] also reported that GO could be reduced to RGO during high-temperature sintering. Maharana et al. [28] added reduced graphene oxide to the pure copper matrix to improve its high-temperature oxidation resistance. In general, the strengthening mechanism of GO doped composites mainly includes the following aspects. First, high-density dislocations occur at the interface due to different thermal expansion coefficients of graphene and copper matrix. Second, the grain boundaries area is increased and grains are refined after graphene doping [29,30]. Furthermore, it is also an efficient strengthening mechanism to enhance the binding force between the graphene and the matrix by forming a small amount of oxides and carbides at the interface. For example, Ke et al. [31] studied the strengthening mechanism of the RGO-reinforced CuCr alloy. It was found that Cr_7C_3 was formed at the interface during sintering, which greatly improved the bond strength.

In summary, graphene oxide can be converted into reduced graphene oxide after sintering, which can enhance the interfacial bond strength, thereby improving the matrix strength. In our previous work, the Al_2O_3-Cu/35W5Cr electrical contact material was investigated. The tensile strength of the sintered samples was 277 MPa, and the welding force was 0.23 N at 30 V DC and 25 A [13]. In order to optimize the mechanical properties and welding resistance of contact materials, the authors tried to add a small amount of graphene oxide into the matrix of Al_2O_3-Cu/35W5Cr contact material. Consequently, GO/Al_2O_3-Cu/35W5Cr contact materials

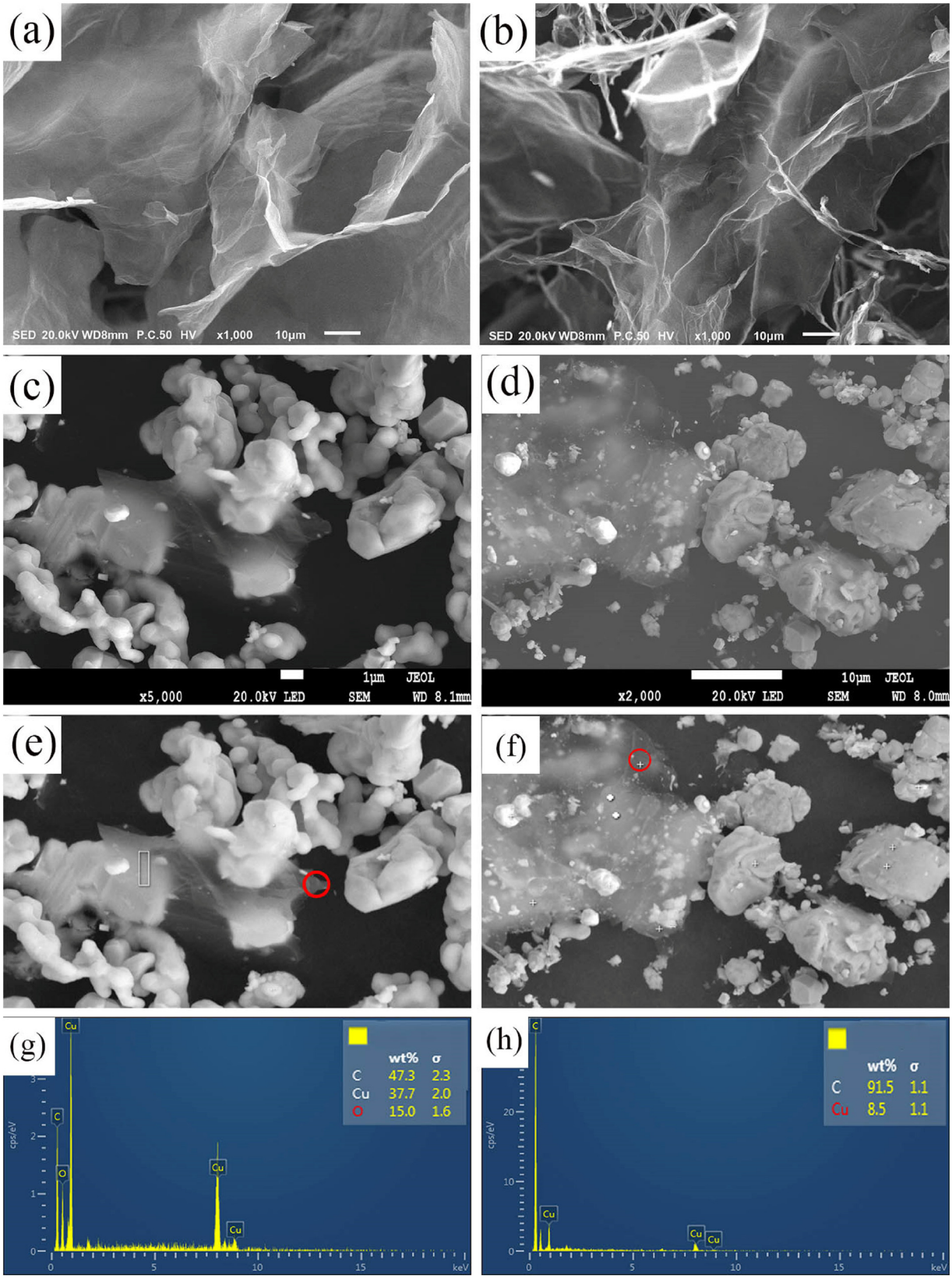

Fig. 3. SEM images of GO and composites powders: (a, b) GO flakes; (c) 0.3GO/Cu-0.4Al/35W5Cr composites powders; (d) 0.5GO/Cu-0.4Al/35W5Cr composite powders; (e, g) EDS results of the 0.3GO/Cu-0.4Al/35W5Cr; (f, h) EDS results of the 0.5GO/Cu-0.4Al/35W5Cr (σ: deviation).

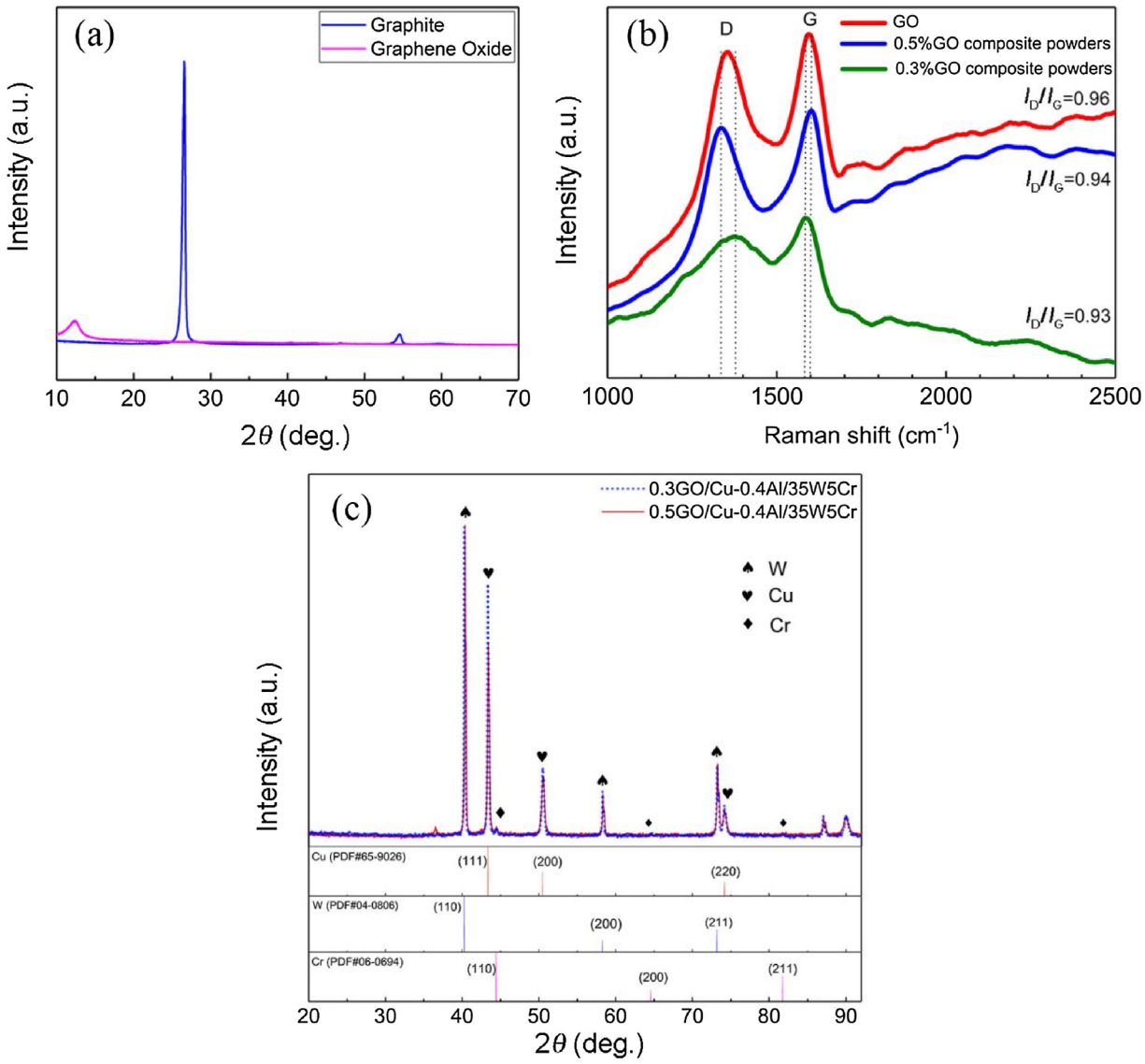

Fig. 4. (a) XRD patterns of graphene oxide and graphite, (b) Raman spectra of different materials and (c) XRD patterns of the composites powder.

were successfully fabricated by vacuum hot-pressing sintering and internal oxidation, which combined particles reinforcement with RGO reinforcement. The electrical conductivity, Brinell hardness and relative density of the GO/Al_2O_3-Cu/35W5Cr composites were measured. Graphene oxide and composite powders were analyzed by X-ray diffraction (XRD) and Raman spectroscopy. X-ray photoelectron spectroscopy (XPS) was used to investigate changes in the GO structure. JEM-2100 transmission electron microscope (TEM) and JSM-7800 F field emission scanning electron microscope (SEM) were used to analyze the samples' microstructure. The Shimadzu AG—I 250 kN precision universal testing machine was used to test different contact materials. Finally, the electrical contact experiments were carried out using the JF04C electrical contact testing system. The effects of different graphene oxide content on the electrical contact properties of different contact materials were analyzed.

2. Experimental

2.1. Preparation of GO-doped composite powders

Cu-0.4 wt% Al powder (≥99.9% purity) with an average size of 38 μm and Cu_2O (≥99.9% purity) particles ranging from 2 μm to 5 μm in size were purchased from the Hua Bang Powder Group Co., Ltd., Hunan, China. W (≥99.9% purity, 2–5 μm average particle size) and Cr (≥99.9% purity, 44 μm average particle size) were provided by the Xing Rong Yuan Technology Co., Ltd., Beijing, China. These four kinds of powders were adequately mixed in the YH-10 mixer (10:1 ball-to-powder weight ratio) at 5 rpm for 2 h in ambient atmosphere. Pure copper balls served as the mixing media to prevent agglomeration of the particles.

Some monolayer flake graphene oxide (≥99% purity, ≥99% monolayer rate, 0.5–5 μm average diameter, 0.8–1.2 nm thickness), purchased from the Xian Feng Nano Materials Technology Co., Ltd., was placed in 1000 ml of deionized water and oscillated for 1 h by the ultrasonic cleaner to obtain the GO suspension. Then a certain amount of premixed powders was added to the suspension. The mixed suspension was transferred to the mill tank with the ball-to-powder ratio of 10:1, and the speed of the ball mill was 360 rpm in an argon atmosphere. After 5 h, the suspension was placed into the Lg-0.2 vacuum freeze dryer. The freezing temperature is -20 °C, and the cold trap temperature was −40 °C. After 24 h, the samples were transferred to the YH-10 mixer (10:1 ball-to-powder weight ratio) at 46 rpm in ambient atmosphere and mixed again for 1 h to obtain the GO/Cu-0.4Al/35W5Cr composites powder (Fig. 2 (a)). Pure copper balls were also employed as the mixing media.

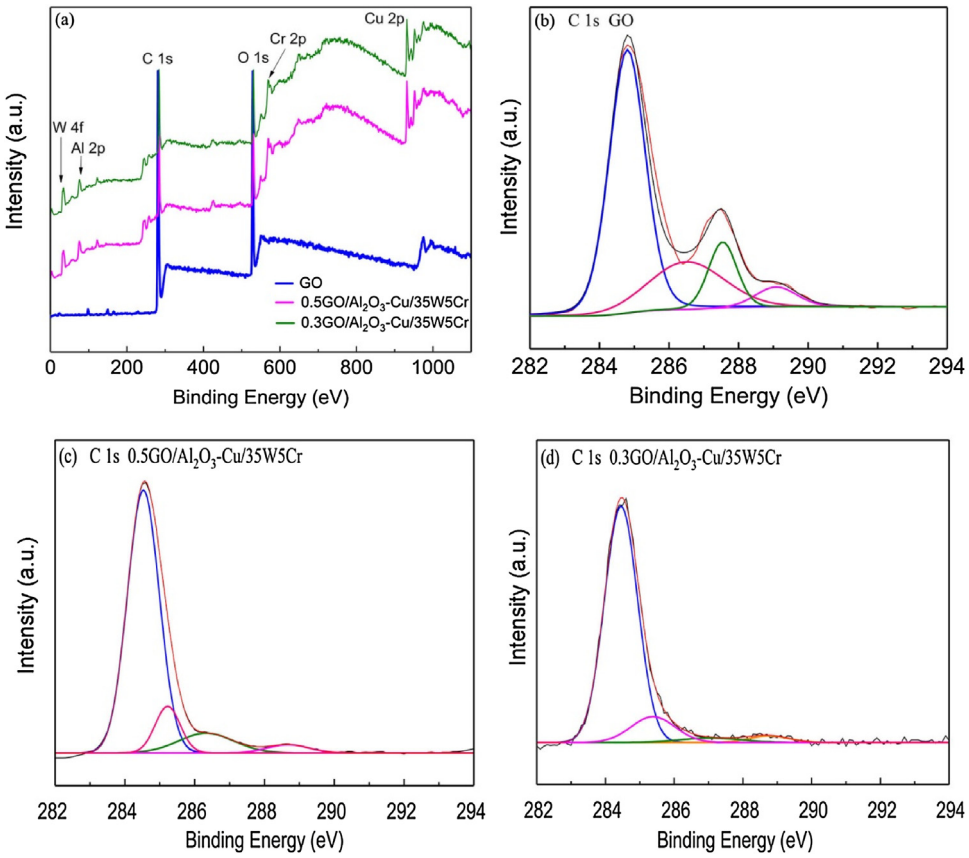

Fig. 5. XPS analysis of the two as-sintered composites: (a) survey scan of GO and the two composites; curve fit of the C 1s spectra of (b) GO, (c) 0.5GO/Al_2O_3-Cu/35W5Cr and (d) 0.3GO/Al_2O_3-Cu/35W5Cr.

Finally, graphene oxide and mixed powders were analyzed by X-ray diffraction (Bruker D8) and Raman spectroscopy (LabRAM Aramis). The scanning electron microscope images of different powders and composition ratios are shown in Fig. 1.

2.2. GO/Al_2O_3-Cu/WCr composites fabrication and characterization

The GO/Cu-0.4Al/35W5Cr mixed powders were loaded into a graphite die. The sintering of the two composites was carried out in the ZT-120-22Y multifunctional sintering furnace (6×10^{-2} Pa vacuum degree and 10 °C/min heating rate). The uniaxial contact pressure of 30 MPa was applied at 600 °C and held for 1 h, followed by heating to 950 °C for 1 h, and then dropped to 100 °C prior to sample removal (Fig. 2(a)). One as-sintered sample was prepared for each kind of composite, and the two as-sintered samples with Φ 50 mm × 10 mm dimensions were obtained.

The Sigma 2008B1 digital instrument was used to measure the electrical conductivity of the as-sintered samples. The electrical conductivity was the average value obtained by measuring the upper surface of the as-sintered samples nine times. Brinell hardness measurements were carried out with the HB-3000B Brinell hardness tester with 2500 N load held for 30 s according to the GB/T231.1–2009 standard, which was performed nine times on the upper surface of the as-sintered samples. Moreover, the relative density was measured and calculated with a MS105 hydrostatic balance using deionized water at 20 °C as a liquid medium. Consequently, the standard deviation for the obtained mean values of these characteristics is listed in Table S1. The JSM-7800 F field emission scanning electron microscope and the JEM-2100 transmission electron microscope were used to analyze the microstructure of the as-sintered samples. In order to investigate the reduction of the GO during the high-temperature sintering process, the X-ray photoelectron spectrometer (Axis Ultra DLD) was used.

2.3. Tensile and arc erosion tests

According to the GB/T228-2002 standard, as-sintered composites were cut into standard samples. Tensile tests were carried out at room temperature using the Shimadzu AG-I 250 kN universal testing machine. The crosshead speed was 1 mm/min and three specimens of each kind were tensile tested to obtain the results.

As-sintered composites were cut into Φ3.8 mm × 10 mm cylindrical specimens and served as the anode and cathode electrical contacts. The contacts surfaces were ground and polished. The specimens were weighed by the FA2004B electronic balance before and after the test with each data point representing the average result of 5 measurements. The formula $\Delta m=m_2-m_1$, where m_2 represents the mass of the contact after testing and m_1 represents the specimen mass before testing, was used to calculate the mass change during arc erosion. Five thousand contact cycles were carried out on the JF04C electrical contact testing apparatus, as shown in Fig. 2(b). These tests were conducted in argon. The bottom contact served as a cathode, while the top contact was an anode. The tests were carried out with the voltage set to 30 V DC and the current of 10, 20, 25, and 30 A, respectively. The contact force was 0.4-0.6 N and the contact breaking frequency was 1 Hz. Each testing group was repeated three times. After testing, the arc erosion morphology of the contacts was analyzed by the JSM-5610LV scanning electron microscope and the three-dimensional profilometer.

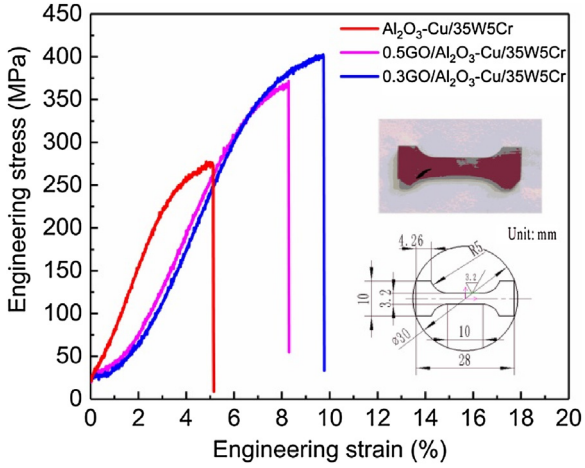

Fig. 6. Tensile stress-strain curves of different composites.

3. Results

3.1. Morphology of GO and composite powders

Pure GO and composite powders containing 0.3 wt% and 0.5 wt% GO were analyzed by scanning electron microscopy, as shown in Fig. 3. It can be seen from Fig. 3(a) and (b) that GO was curled after ultrasonic dispersion and vacuum freeze-drying. Graphene oxide sheets can be observed in both composites powders in Fig. 3(c) and (d). The EDS point scanning mode analysis was used to confirm the composition of the GO, which is shown in Fig. 3(g)-(h). The flake graphene oxide sheets in the composite powders preserved their intact structure after milling and freeze drying. The surfaces of the flakes are coated with copper and W powder, and the rest of the powders are distributed uniformly without obvious agglomeration.

3.2. XRD and Raman spectra analysis

Fig. 4(a) shows the XRD pattern of natural graphite and GO. The two curves present two sharp diffraction reflections at 26.5° and 12°. They correspond to the characteristic diffraction of natural graphite (JCPDS ICCD card No. 41-1487) and graphene oxide, respectively [32]. The diffraction intensity can reflect the crystallinity of the materials. Compared with GO, the diffraction reflections of natural graphite are higher and narrower, indicating that the original crystal structure of graphene oxide has been destroyed due to the existence of functional groups.

Raman spectroscopy is an effective characterization method to investigate the molecular structure of carbon materials. Fig. 4(b) shows the Raman spectra of the pure GO and the composite powders with different GO contents. As shown in Fig. 4(b), the D and G bands of graphene oxide appear at ~1355 cm^{-1} and ~1596 cm^{-1}, respectively. The peak at 1355 cm^{-1} is the defects peak, which is caused by breaks in the translational symmetry of the hexagonal lattice and reflects the defects and disorder levels of graphene oxide. In addition, the G band at 1596 cm^{-1} is caused by the C—C tangential vibration, which reflects the symmetry of GO. The intensity ratio of I_D/I_G is usually used to characterize the defects density of graphene and its derivatives [33,34]. After milling and freeze-drying, the D and G bands of the two composites powders show a slight shift compared with GO. The I_D/I_G values of GO and the other two kinds of composites powders are 0.96, 0.94 and 0.93, respectively. Thus, these results indicate that graphene oxide can still maintain its original structure after dispersing, ball milling and freeze-drying.

In order to investigate the changes of the composites powder in the milling process, the phase structure of the composites powder was determined by XRD. As shown in Fig. 4(c), the X-ray diffraction reflections at $2\theta = 43.3°$, 50.5°, 74.2°, and 89.9° correspond to the (111), (200), (220), and (311) planes of Cu (JCPDS ICCD card No. 65–9026). In addition, the reflections of tungsten at $2\theta = 40.3°$, 58.3°, 73.2°, and 87° correspond to the (110), (200), (211), and (220) planes (JCPDS ICCD card No. 04-0806). Nevertheless, two weak diffraction reflections emerged at $2\theta = 44.3°$ and 81.7°, which correspond to the (110) and (211) planes of Cr (JCPDS ICCD card No. 06-0694). Furthermore, due to the formation of a supersaturated solid solution during milling, the intensity of the Cr reflections weakened.

3.3. XPS analysis of GO and composites

X-ray photoelectron spectroscopy is often used to characterize the chemical structure and composition of graphene and its derivatives. Not only it reveals the elemental composition of samples, but also illustrates the percentage of different oxygen-containing functional groups. Fig. 5(a) is the survey scan spectra of GO and the two composites. Based on the different peaks in the XPS spectra, both composites exhibit W 4f peak, Al 2p peak, C 1s peak, O 1s peak, Cr 2p peak, and Cu 2p peak, respectively. The corresponding binding energy is around 31 eV, 75 eV, 284 eV, 530 eV, 580 eV, and 932 eV, respectively. The Cu 2p spectra, W 4f spectra, Cr 2p spectra, and Al 2p spectra are shown in Fig. S1. The different states and oxidation levels of carbon atoms in the composites can be obtained from the C 1s spectra, which are shown in Fig. 5(b)-(d). After the C 1s spectra were fitted, the characteristic signal peaks of GO on the C 1s spectrum located at 284.5 eV, 286.4 eV, 287.5 eV, and 289.1 eV, correspond to the sp^2 and sp^3 C—C, C—O, C═O and O═C—O carbon bonds, respectively [35–37]. In order to investigate the reduction of GO during the vacuum hot-pressing sintering process, the atomic concentrations of different carbon bonds were calculated. As shown in Table S2, compared with GO, the percentages of the sp^2 and sp^3 C-C bond in two composites increase, while the total percentages of the other bonds decrease sharply. This indicates that most of GO was reduced into RGO during the vacuum hot-pressing sintering process, which is significant for enhancing its electrical conductivity.

3.4. Mechanical properties of composites

Table S1 shows the comprehensive properties and tensile strength of the different composites. The relative density values were obtained according to the following analysis. The theoretical density of the as-sintered samples was calculated according to the following formula:

$$\rho_t = \frac{m_1 + m_2 + m_3 + m_4 + m_5}{\frac{m_1}{\rho_1} + \frac{m_2}{\rho_2} + \frac{m_3}{\rho_3} + \frac{m_4}{\rho_4} + \frac{m_5}{\rho_5}} \quad (1)$$

where ρ_t is the theoretical density value, m_1, m_2, m_3, m_4, m_5 are the masses of Cu-0.4Al powder, W powder, Cr powder, Cu_2O powder, and graphene oxide, respectively. ρ_1, ρ_2, ρ_3, ρ_4, ρ_5 refer to the corresponding density of different powders. The realized density of the as-sintered samples was calculated according to the following formula:

$$\rho_r = \frac{\rho_w m_a}{m_a - m_w} \quad (2)$$

where ρ_r is the realized density value, m_a and m_w are the masses of the as-sintered sample, which was weighed in the air and the deion-

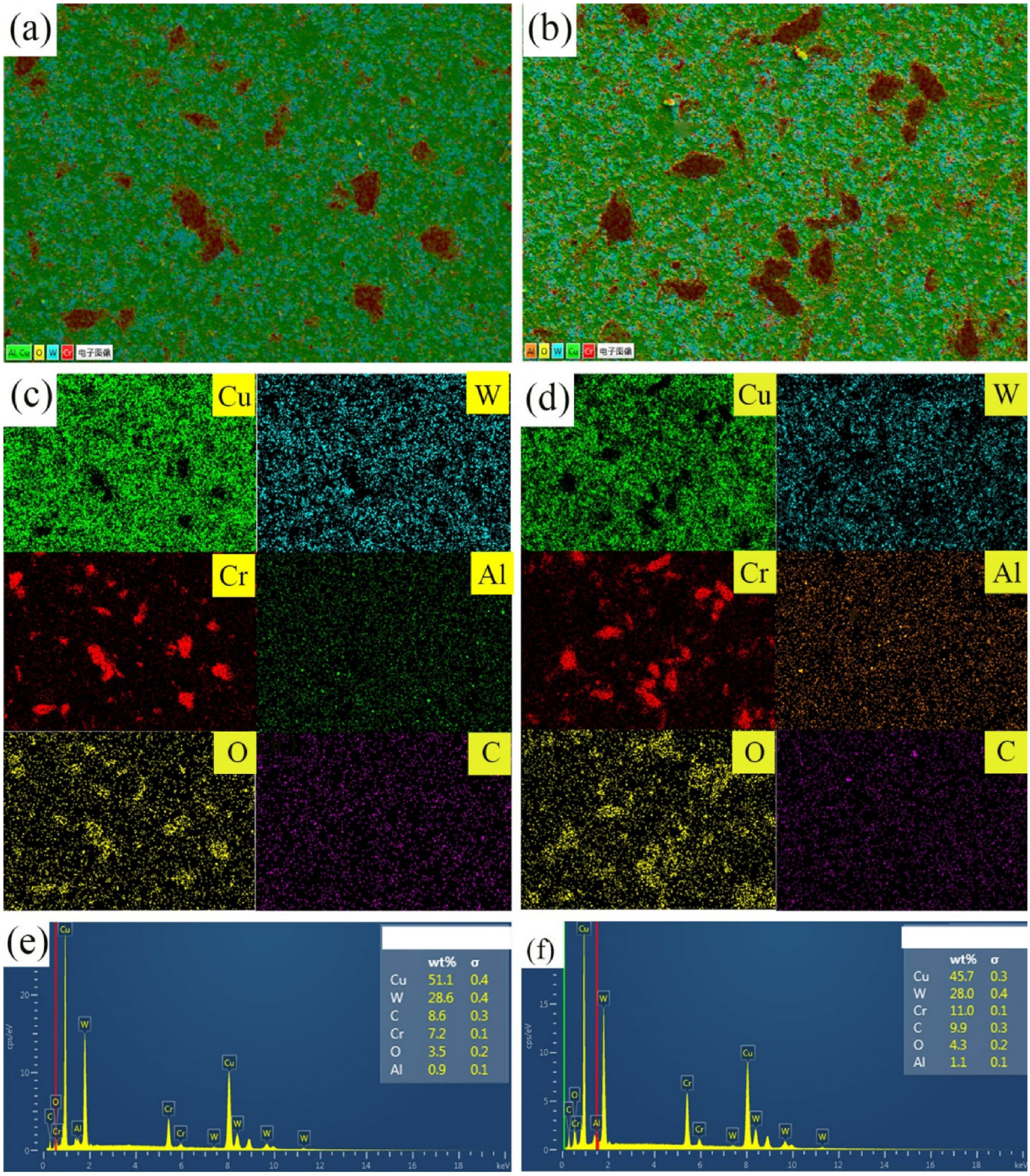

Fig. 7. SEM images and corresponding EDS maps of the two composites: (a, c, e) 0.3GO/Al_2O_3-Cu/35W5Cr; (b, d, f) 0.5GO/Al_2O_3-Cu/35W5Cr.

ized water, respectively. Consequently, relative density values can be obtained as follows:

$$R = \frac{\rho_r}{\rho_t} \times 100\% \quad (3)$$

As calculated, the relative density of the 0.3GO/Al_2O_3-Cu/35W5Cr and 0.5GO/Al_2O_3-Cu/35W5Cr contact materials is above 98.5%. Moreover, compared with the Al_2O_3-Cu/35W5Cr prepared by the same process, the electrical conductivity of the other two kinds of composites gradually increased to 68.4 ± 0.32%IACS and 64.5 ± 0.58%IACS in Table S1, respectively. Although the conductivity of graphene oxide is very poor, some functional groups can be reduced and transformed into reduced graphene oxide with better conductivity in the sintering process [24]. In addition, GO was not reduced completely according to the XPS analysis results. However, the effect of the RGO on the conductivity plays a more significant role than GO. Consequently, the electrical conductivity of the composites doped with GO increased. Furthermore, the composite doped with 0.5 wt% GO has lower electrical conductivity due to the agglomeration of GO. Besides, Brinell hardness of the two composites doped with GO increased by 14% and 19%, respectively. Dispersed nano-Al_2O_3 and Cr_3C_2 particles can hinder dislocations motion and improve the hardness of the composites in addition to the strengthening effects of RGO.

The adequate mechanical properties requirement must be satisfied for the good electrical contacts. The welding resistance of

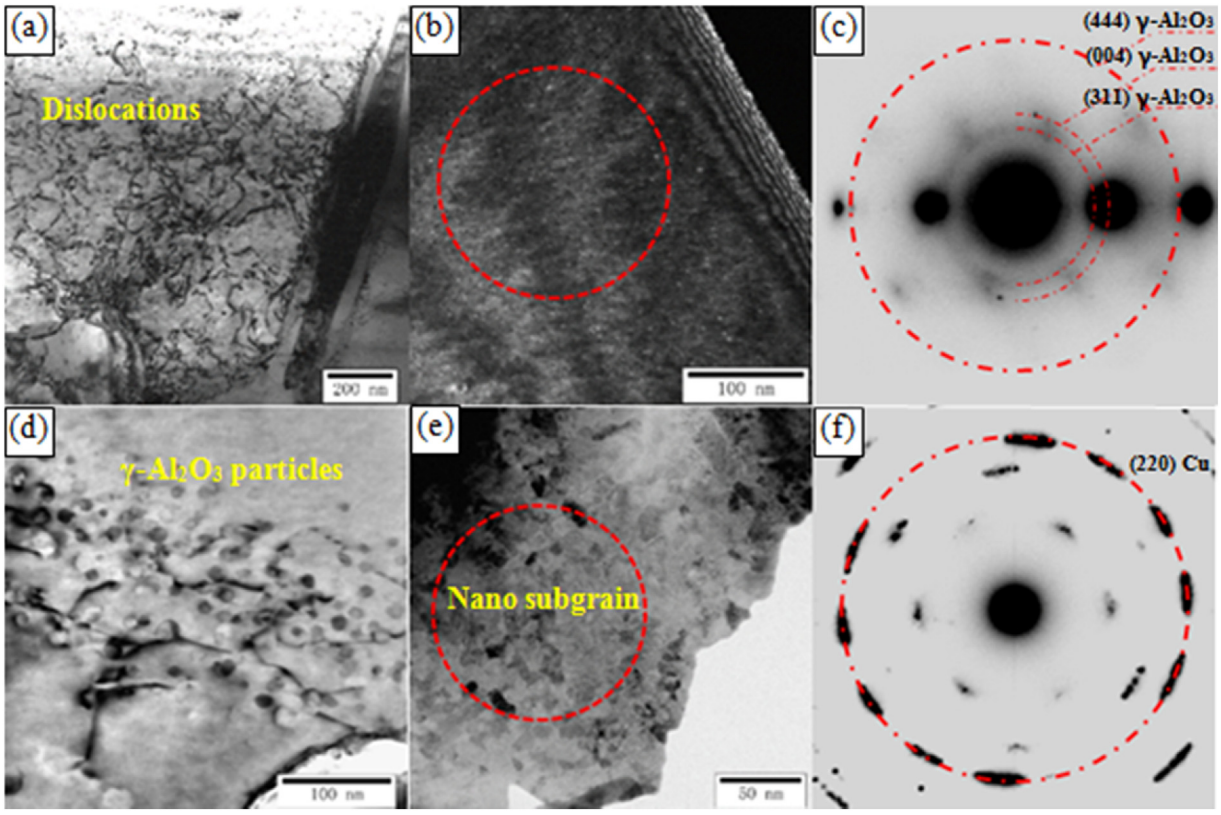

Fig. 8. TEM images of 0.5GO/Al_2O_3-Cu/35W5Cr composite: (a, b, d, e) TEM images; (c) SADP image of (b); (f) SADP image of (e).

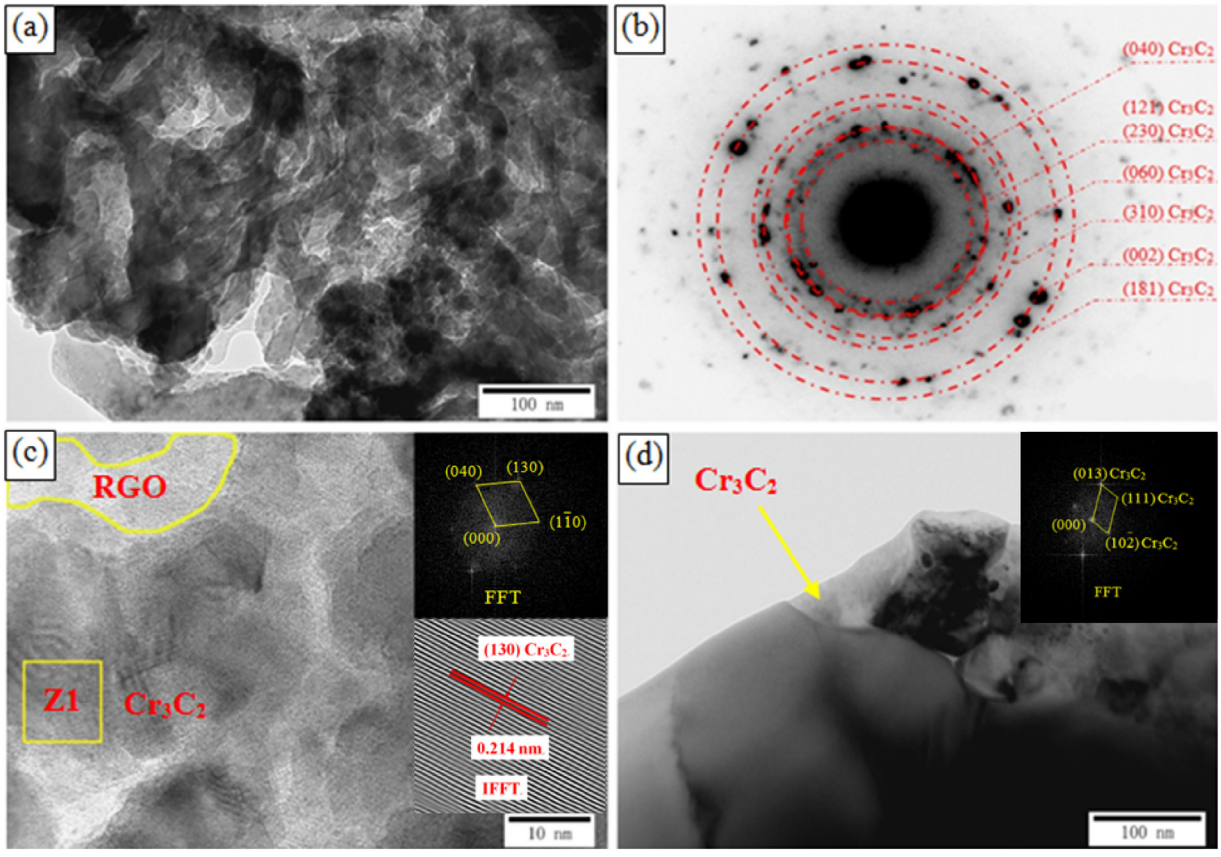

Fig. 9. TEM images of 0.5GO/Al_2O_3-Cu/35W5Cr composite: (a, d) TEM images; (b) SADP image of (a); (c) HRTEM image of Cr_3C_2 formed on the RGO and FFT, IFFT of Z1.

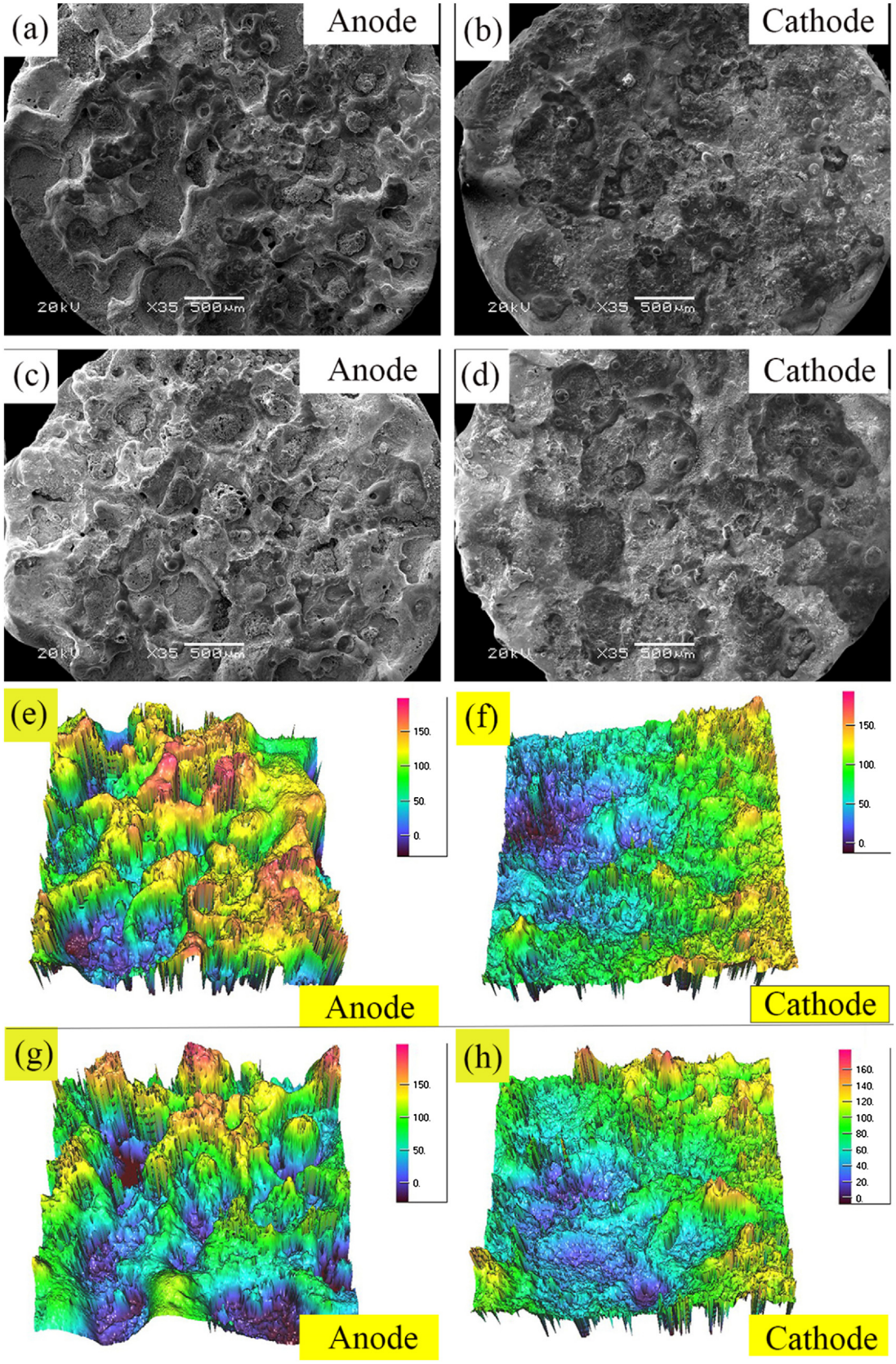

Fig. 10. Low-magnification SEM images and corresponding three-dimensional profile: (a, b, e, f) 0.3GO/Al_2O_3-Cu/35W5Cr; (c, d, g, h) 0.5GO/Al_2O_3-Cu/35W5Cr.

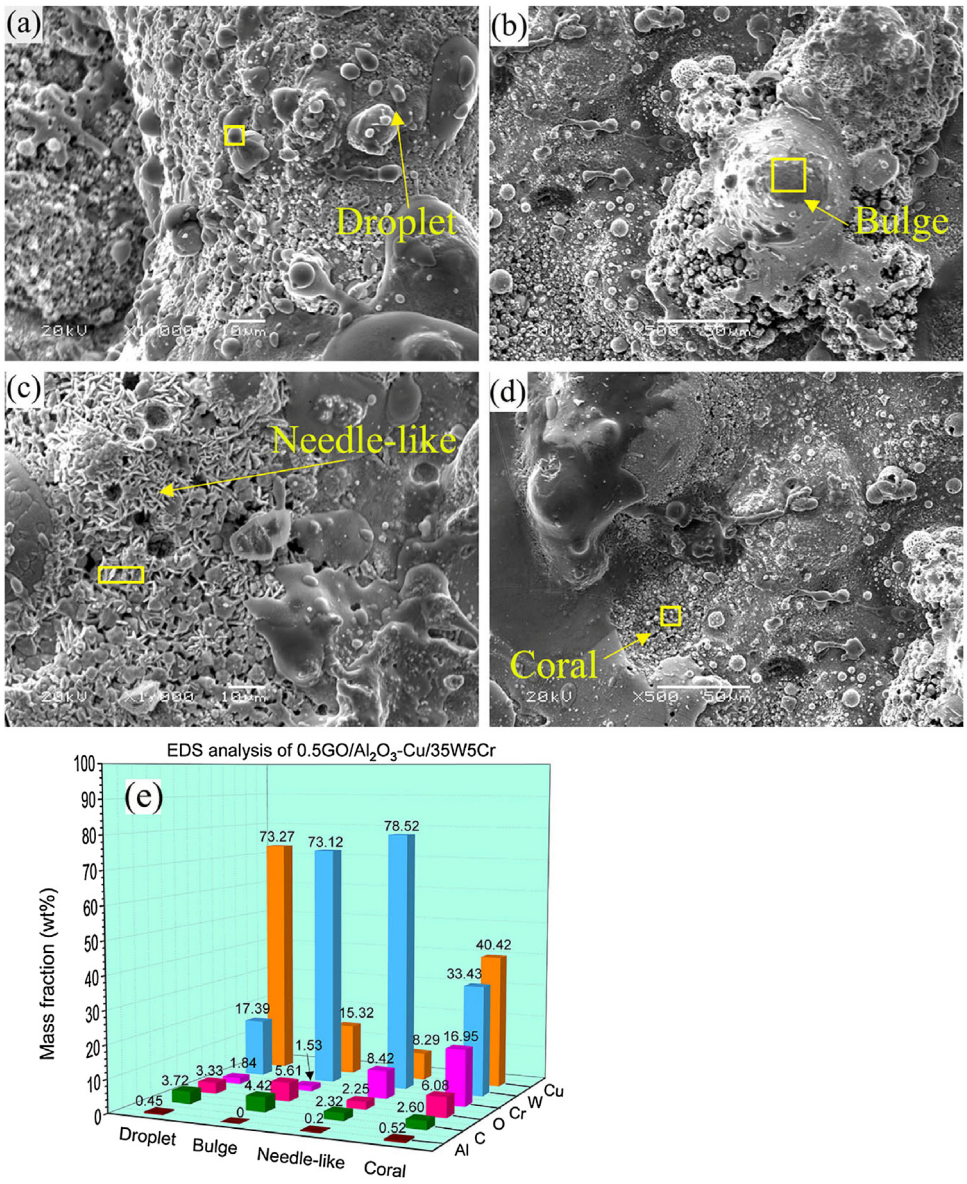

Fig. 11. High magnification SEM images of arc erosion morphology and elemental analysis of four boxed areas: (a) droplet; (b) bulge; (c) needle-like skeletons; (d) coral; (e) EDS data.

electrical contacts is related to the tensile strength of the contact material, since the lower the tensile strength, the lower the welding force [38]. Nevertheless, too low tensile strength will lead to a decline in mechanical wear performance of electrical contacts. The tensile test results of the Al_2O_3-Cu/35W5Cr, 0.3GO/Al_2O_3-Cu/35W5Cr, and 0.5GO/Al_2O_3-Cu/35W5Cr composites are shown in Fig. 6. The tensile strength of the three composites is 277 ± 5.09 MPa, 403 ± 5.88 MPa, and 371 ± 4.32 MPa, respectively. Compared with the Al_2O_3-Cu/35W5Cr composite, the tensile strength of the composites doped with GO increased by 45% and 34%, respectively. This suggests that the best strengthening effect was obtained by adding 0.3 wt% GO under current experimental conditions. The strengthening mechanism of graphene oxide is as follows. First, graphene oxide loses some functional groups at high temperature and forms high-density dislocations at the interface due to the difference of thermal expansion coefficient between the reduced graphene oxide and the matrix. Second, a small amount of C and Cr form Cr_3C_2, which optimized the bond interface and caused work hardening.

3.5. Microstructure of composites

The SEM images of the 0.3GO/Al_2O_3-Cu/35W5Cr and 0.5GO/Al_2O_3-Cu/35W5Cr composites are shown in Fig. 7. In Fig. 7, W and Cr particles are distributed on the dispersed copper matrix uniformly without obvious agglomeration. Besides, the surfaces of the matrix are compact without voids.

Fig. 8 shows the TEM images of the 0.5GO/Al_2O_3-Cu/35W5Cr composite. It can be seen that the high dislocation density is preserved in the copper matrix after vacuum hot pressing sintering in Fig. 8(a). Many dispersed nanoparticles in Fig. 8(b) and (c) were formed in situ in the matrix. The selected area electron diffraction pattern in Fig. 8(c) illustrates that the γ-Al_2O_3 nano-particles formed in situ by internal oxidation. In Fig. 8(d), dislocations were pinned by the γ-Al_2O_3 particles. They have a strong pinning effect, and hinder dislocation movement, thereby improving the strength of the copper matrix. Furthermore, the nano-subgrains are also observed in the copper matrix in Fig. 8(e) and (f). This indicates that the Cu matrix has not completely recrystallized after hot-pressing sintering at 950 °C, and high dislocation density still exists in some

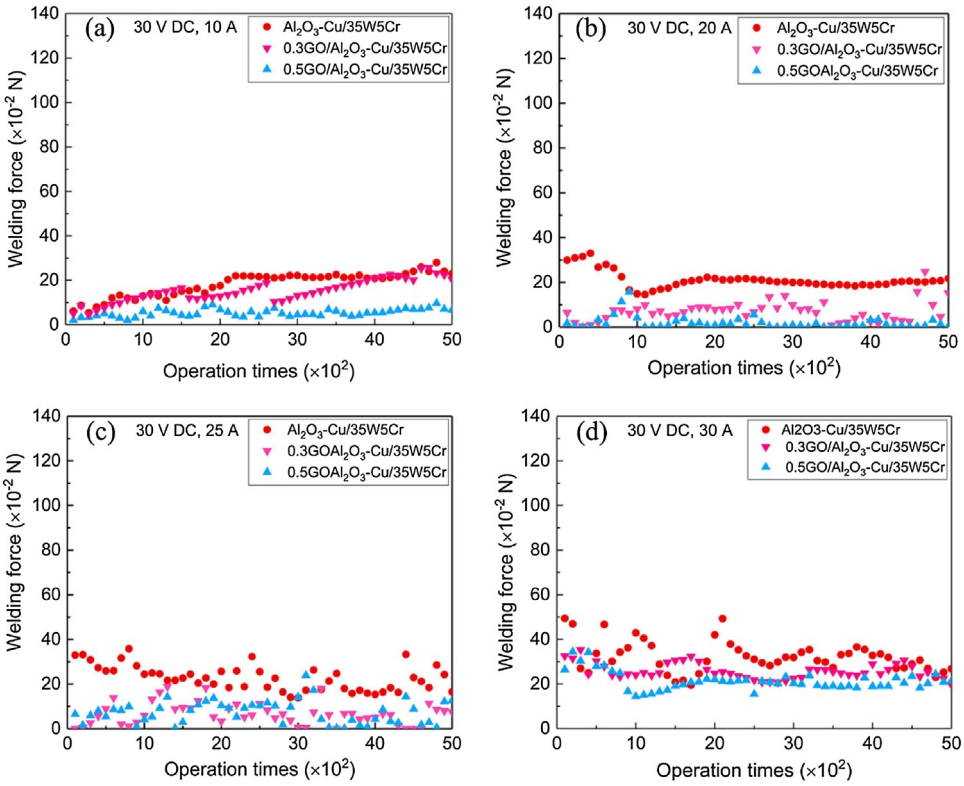

Fig. 12. Welding forces of different composites at (a) 30 V DC, 10 A, (b) 30 V DC, 20 A, (c) 30 V DC, 25 A and (d) 30 V DC, 30 A.

areas of the matrix. However, recovery occurred in some areas, resulting in the formation of nano-scale subgrains with an average size of about 20 nm.

Fig. 9 shows the TEM and HRTEM images of the 0.5GO/Al_2O_3-Cu/35W5Cr composite. In Fig. 9(a) and (c), some in situ formed particles adhere to the corrugated RGO flakes. The selected area electron diffraction pattern in Fig. 9(b) shows the Cr_3C_2 particles. In addition, the selected region in Fig. 9(c) marked as Z1 was analyzed by using the fast Fourier transform and verified that the carbides particles were Cr_3C_2. The same phase had been identified in Fig. 9(d). Cr_3C_2 has high hardness, good wettability with Cu and strong oxidation resistance. Thus, these Cr_3C_2 particles play a significant role in enhancing the interface bonding and coupling the RGO and Cu. This results in the significant enhancement of the mechanical properties.

3.6. Arc erosion morphology

In the process of making and breaking the circuit, the contacts are affected by the thermal-mechanical action of the arc energy. Due to the arc discharge, the great heat flow causes the contact surface melting, vaporizing, and even sputtering, which is defined as “arc erosion” [39]. Under the arc action, the great heat flux makes the metal melt on the contacts surface, and then the liquid metal flows on the surface under the thermal-mechanical action. The flow of liquid metal leads to the segregation of the composite composition on the contact surface. Moreover, the reason for liquid splashing is the effect of the electrode force on the liquid metal, which includes spot pressure, electrostatic and electromagnetic forces [40]. Fig. 10 shows the low-magnification images and corresponding three-dimensional profile of the two kinds of GO-doped contacts after 5000 cycles under 30 V DC and 30 A. It can be seen from Fig. 10 that some hills and craters were formed on the anode and cathode surfaces.

Fig. 11 shows the high-magnification erosion morphologies of the 0.5GO/Al_2O_3-Cu/35W5Cr along with the energy dispersive spectrometry (EDS) analysis results. From Fig. 11(a)–(d), typical arc erosion morphology, such as scattered droplets, spiral protrusions, needle-like skeleton, and coral-like structures, appears on the electrodes’ surfaces. Due to the high temperature of the arc, copper melts and splashes to form droplets or spreads after solidification, which results in the erosion of large amount of copper in Fig. 11(a) and (b). The W particles undergo the process of resintering at high temperature to form needle-like structures in Fig. 11(c), which can restrict the flow of liquid and thus reduce the splashing of materials [41]. This phenomenon has been verified in our previous research [13]. Besides, the surface of the contacts is uneven due to the splashing flow of molten metal and the fracture of the metal bridge. In addition, the accumulation of refractory metals leads to the appearance of the coral-like structure, shown in Fig. 11(d).

3.7. Welding resistance

Welding is one of the main failure modes of electrical contacts. When arcing occurs due to the contacts breakdown or bouncing, their surfaces can melt at high temperature. After arcing, the melted materials solidify and hold the contacts connected, which is called welding [42]. The force required for separating the welded contacts is the welding force. Fig. 12 shows the welding force of different composites under the 30 V DC, 10–30 A test conditions, with each data point representing the average result of 100 breaking operations. As shown in Fig. 12, as the current increases, the welding force of the three composites increases. Furthermore, it is noteworthy that the 0.5GO/Al_2O_3-Cu/35W5Cr has the least welding force under all conditions. For instance, at 30 V DC, 25 A, the welding force values of the three composites are 0.23 N, 0.073 N and 0.067 N,

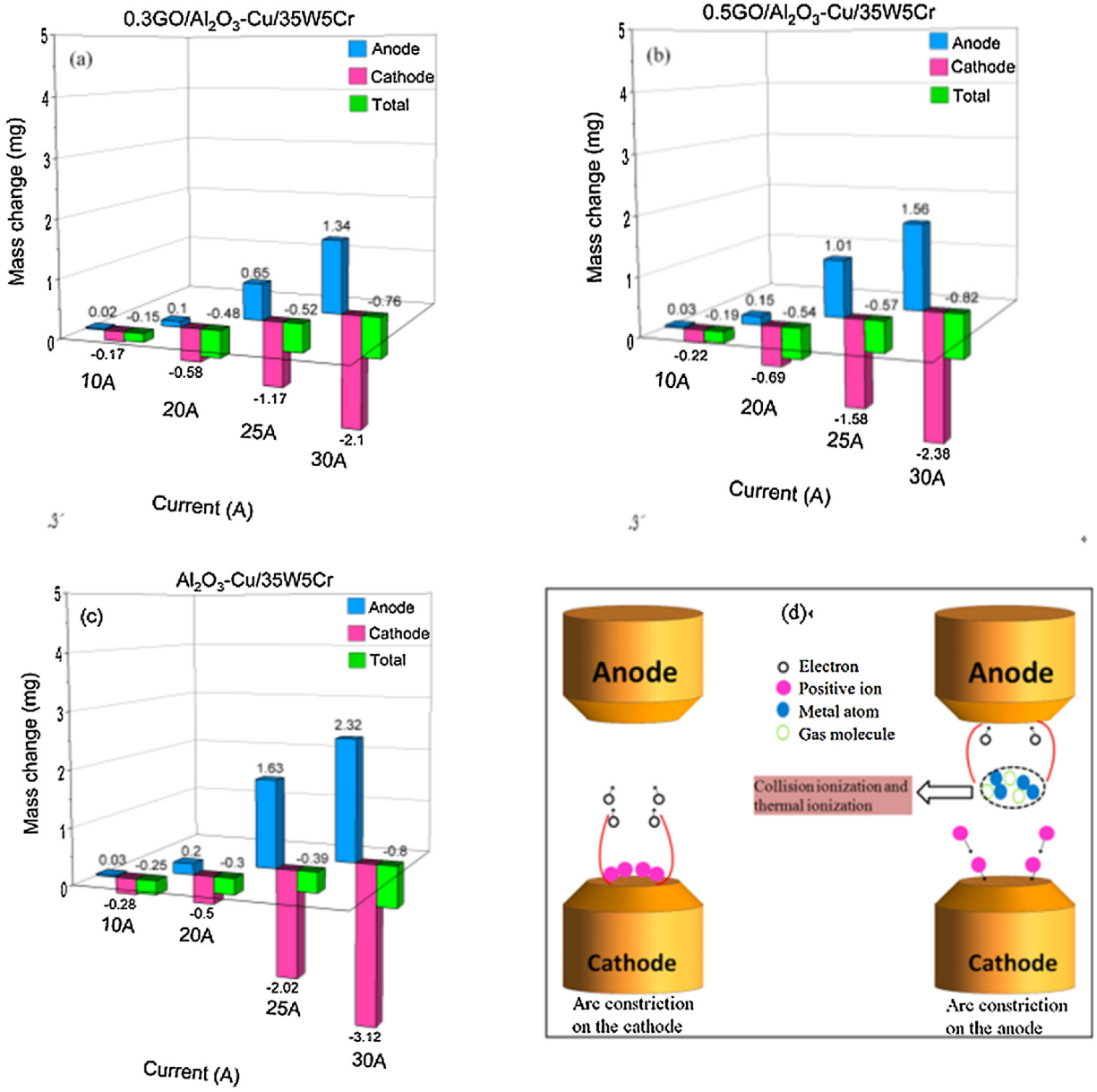

Fig. 13. (a) Mass change of the 0.3GO/Al_2O_3-Cu/35W5Cr composite, (b) mass change of the 0.5GO/Al_2O_3-Cu/35W5Cr composite, (c) Mass change of the Al_2O_3-Cu/35W5Cr composite and (d) schematic of the different particles movement under different conditions.

respectively. When the GO content in the copper matrix composites was increased from 0.3 wt% to 0.5 wt%, the welding resistance improved.

The reasons can be explained as follows. First, the hardness and brittleness of the material have an important influence on the welding resistance. The higher the material hardness, the better welding resistance can be obtained. The 0.5GO/Al_2O_3-Cu/35W5Cr composite has high hardness resulting in better welding resistance. In addition, the other aspect is that the lower the tensile strength of the contact material, the better the welding resistance it has. Furthermore, the welding resistance is related to the welding tendency and the welding force. Different materials have different welding tendency. After analysis of the welding tendency and welding force of different materials, Liu and Fei [43] proposed the following mathematical models:

$$k_w = \frac{\varphi_e T_m \sqrt{C\rho\lambda}}{{\varphi_i}^2 \varphi_a} \tag{4}$$

$$F = k\left(0.75\sqrt{\pi}\, I \cdot t_a\right)^{2/3} \cdot \sigma \left[\frac{\varphi_i}{\rho\left(3CT_m + H_m + \frac{H_v}{\sqrt{27}}\right)}\right]^{2/3} \tag{5}$$

where φ_a and φ_e are the work functions of the anode and the cathode, respectively. T_m is the melting point, C is the specific heat, and λ is the thermal conductivity. H_m and H_v are latent heats of fusion and vaporization, respectively. k_w and F are the welding tendency and welding force, respectively. Higher k_w indicates better welding resistance. Based on Eqs. (4) and (5), higher ρ, T_m, C_P, H_m, H_v and λ values result in better welding resistance of electrical contact material. Consequently, the combined effects of the above several aspects determined the final welding resistance of the composites.

4. Discussion

The transfer or loss of contact material directly affect the service life of electrical contacts and lead to component failure. When the

arc is generated, the material is separated from the electrodes by evaporation, liquid spatter or detachment. Fig. 13(a)–(c) shows the mass change trends of the 0.3GO/Al_2O_3-Cu/35W5Cr, 0.5GO/Al_2O_3-Cu/35W5Cr and Al_2O_3-Cu/35W5Cr contacts after electrical contact tests under 30 V DC and 10–30 A conditions. It can be seen from Fig. 13(a)–(c) that the mass transfer of the composites was from the cathode to the anode. Furthermore, the total mass change of the two composites was negative, indicating material loss to the environment. Since the current is low, there are less charged particles produced by ionization. The maintenance of arc mainly depends on the accumulation of cations on the cathode surface and the shrinkage of the arc in the cathode area to compensate for the shortcomings of the electric field emission. Finally, the aggregation of cations and the shrinkage of the arc in the cathode area increase the heat flux of the arc input cathode and the material transfers from the cathode to the anode [44,45].

In our previous work, the mass change of the Al_2O_3-Cu/25W5Cr composites had an obviously decreasing trend at 30 A due to the probability of collision ionization and increased thermal ionization. Maintaining the arc no longer depends on the arc constriction in the cathode area and ionization of the electrons. Consequently, the arc constriction phenomenon in the cathode area disappeared. In order to maintain the arc and the lowest arc voltage, the arc column in the anode area was constricted, resulting in a small amount of material transfer from the anode to the cathode. However, when the tungsten content increases to 35 wt% in the GO/Al_2O_3-Cu/35W5Cr composites, the increase of charged particles to maintain arc is not enough at high current due to the high melting point and low saturated vapor pressure of tungsten. It still needs to rely on the aggregation of cations and the shrinkage of cathode arc to maintain the arc. The phenomenon of material transfer from the anode to the cathode cannot happen. Therefore, the materials of the two composites have to transfer from the cathode to the anode, and the mass change increases consistently from 10 A to 30 A. These two different mechanisms are illustrated in Fig. 13(d). In addition, the mass transfer of contacts containing 0.5 wt% GO is greater than the contacts containing 0.3 wt% GO at each current. The reason is that contacts containing 0.5 wt% GO have lower electrical conductivity, which has been shown in Fig. 6. Thus, more heat generated by the arc cannot be effectively dispersed and leads to deeper contacts erosion.

5. Conclusion

Vacuum freeze-drying is used to dry the mixed suspension of composites powders doped with graphene oxide. It can preserve the structure of graphene oxide more completely and reduce the level of agglomeration. Vacuum hot-press sintering and internal oxidation method were combined to fabricate the 0.3GO/Al_2O_3-Cu/35W5Cr and 0.5GO/Al_2O_3-Cu/35W5Cr composites. The nano-Al_2O_3 particles were formed in situ and pinned the dislocations. In situ formed Cr_3C_2 enhances the interface bonding by obtaining a coupling effect as well as causing working hardening. Brinell hardness of the two composites doped GO increased by 14% and 19%, respectively. The tensile strength of the composites doped with GO increased by 45% and 34%, respectively. Some hills and craters were formed on the anode and cathode surfaces, respectively. The W particles underwent the process of re-sintering at high temperature to form needle-like structures. The material transfer direction of the two composites was from the cathode to the anode. The 0.5GO/Al_2O_3-Cu/35W5Cr composites have the best welding resistance.

Acknowledgments

This work was supported financially by the Open Cooperation Project of Science and Technology of the Henan Province (No. 182106000018), the Henan University Scientific and Technological Innovation Talent Support Program (No. 18HASTIT024), the National Natural Science Foundation of China (U1704143) and the National Science Foundation (No. IRES 1358088).

Appendix A. Supplementary data

Supplementary material related to this article can be found, in the online version, at doi:https://doi.org/10.1016/j.jmst.2019.08.014.

References

[1] S.S. Feng, H.R. Geng, Z.Q. Guo, J. Funct. Mater. 42 (2008) 106–109.
[2] V. Cosovic, A. Cosovic, N. Talijan, D. Zivkovic, D. Manasijevic, D. Minic, J. Alloys. Compd. 567 (2013) 33–39.
[3] R. Nachiketa, K. Bernd, M. Timo, F. Ludo, V. Kim, V. Jef, Mater. Des. 85 (2015) 412–422.
[4] D.B. Xiong, M. Cao, Q. Guo, Z.Q. Tan, G.L. Fan, Z.Q. Li, D. Zhang, ACS Nano 9 (2015) 6934–6943.
[5] B.J. Wang, Y. Zhang, B.H. Tian, V. Yakubov, J.C. An, A.A. Volinsky, Y. Liu, K.X. Song, L.H. Li, M. Fu, J. Alloys. Compd. 781 (2019) 118–130.
[6] Z. Zhao, Y. Zhang, B.H. Tian, Y.L. Jia, Y. Liu, K.X. Song, A.A. Volinsky, J. Alloys. Compd. 797 (2019) 1327–1337.
[7] M.Z. Rong, Electrical Contact Theory, China Machine Press, Beijing, 2004 (in Chinese).
[8] Y.S. Cui, Y. Wang, W.Z. Shao, L. Zhen, V.V. Ivanov, 52th IEEE Holm Conference, IEEE Holm Electrical Contact Conference Committee, Canada, September 25-27, 2006.
[9] W.J. Li, W.Z. Shao, N. Xie, L. Zhang, Y.R. Li, M.S. Yang, B.A. Chen, Q. Zhang, Q. Wang, L. Zhen, J. Alloys. Compd. 743 (2018) 697–706.
[10] K. Song, X. Guo, S. Liang, P. Zhao, Y. Zhang, Mater. Sci. Technol. 30 (2014) 171–175.
[11] X.H. Zhang, Y. Zhang, B.H. Tian, Y.L. Jia, Y. Liu, K.X. Song, A.A. Volinsky, Vacuum 164 (2019) 361–366.
[12] B.H. Tian, P. Liu, K.X. Song, Y. Li, Y. Liu, F.Z. Ren, J.H. Su, Mater. Sci. Eng. A 435–436 (2006) 705–710.
[13] X.H. Zhang, Y. Zhang, B.H. Tian, J.C. An, Z. Zhao, A.A. Volinsky, Y. Liu, K.X. Song, Compos. Part B Eng. 160 (2019) 110–118.
[14] C. Nicolle, D. Mazzucchi, J.P. Gauthier, F. Gentils, 24 th ISDEIV, IEEE Holm Electrical Contact Conference Committee, Germany, August 30-September 3, 2010.
[15] M.B. Schulman, P.G. Slade, L.D. Loud, W.P. Li, Electr. Contacts. Proc. Annu. Holm. Conf. Electr. Contacts 22 (1999) 405–413.
[16] E.D. Taylor, 51th IEEE Holm Conference, IEEE Holm Electrical Contact Conference Committee, USA, September 26–28, 2005.
[17] S.C. Tjong, Mater. Sci. Eng. R. 74 (2013) 281–350.
[18] C. Lee, X. Wei, J.W. Kysar, J. Hone, Science 321 (2008) 385–388.
[19] Y.X. Tang, X.M. Yang, R.R. Wang, M.X. Li, Mater. Sci. Eng. A 599 (2014) 247–254.
[20] T. Varol, A. Canakci, Met. Mater. Int. 21 (2015) 704–712.
[21] L.L. Dong, W.G. Chen, C.H. Zheng, N. Deng, J. Alloys. Compd. 695 (2017) 1637–1646.
[22] A.M. Dimiev, J.M. Tour, ACS Nano 8 (2014) 3060–3068.
[23] Y.W. Zhu, S.T. Murali, W.W. Cai, X.S. Li, J.W. Suk, J.R. Potts, R.S. Ruoff, Adv. Mater. 22 (2010) 3906–3924.
[24] O.C. Compton, S.B.T. Nguyen, Small 6 (2010) 711–723.
[25] A.M. Dimiev, S. Eigler, Graphene Oxide: Fundamentals and Applications, China Machine Press, Beijing, 2018 (in Chinese).
[26] C. Ramirez, L. Garzón, P. Miranzo, M.I. Osendi, C. Ocal, Carbon 49 (2011) 3873–3880.
[27] H.Y. Xia, X. Zhang, Z.Q. Shi, C.J. Zhao, Y.F. Li, J.P. Wang, G.J. Qiao, Mater. Sci. Eng. A 639 (2015) 29–36.
[28] H.S. Maharana, S. Jena, A. Basu, K. Mondal, Surf. Coat. Technol. 345 (2018) 140–151.
[29] B. Chen, J. Shen, X. Ye, H. Imai, J. Umeda, M. Takahashi, K. Kondoh, Carbon 114 (2016) 198–208.
[30] D.D. Zhang, Z.J. Zhan, J. Alloys. Compd. 654 (2016) 226–233.
[31] K. Chu, F. Wang, Y.B. Li, X.H. Wang, D.J. Huang, H. Zhang, Carbon 133 (2018) 127–139.
[32] P. Cui, J.H. Lee, E. Hwang, H. Lee, Chem. Commun. 47 (2011) 12370–12372.
[33] A.C. Ferrari, J.C. Meyer, V. Scardaci, C. Casiaghi, M. Lazzeri, F. Mauri, S. Piscanec, D. Jiang, K.S. Novoselov, S. Roth, A.K. Geim,Phys. Rev. Lett. 97 (2006), 187401.

[34] P. Miranzo, C. Ramirez, B.R. Manso, L. Garzon, H.R. Gutierrez, M. Terrones, C. Ocal, M.I. Osendi, M. Belmonte, J. Eur. Ceram. Soc. 33 (2013) 1665–1674.
[35] Q. Zhang, C. Cai, J.W. Qin, B.Q. Wei, Nano Energy 4 (2014) 14–22.
[36] D.X. Yang, A. Velamakanni, G. Bozoklu, S.J. Park, M. Stoller, R.D. Piner, S. Stankovich, I. Jung, D.A. Field, C.A. Ventrice Jr, R.S. Ruoff, Carbon 47 (2009) 145–152.
[37] Y.X. Tang, X.M. Yang, R.R. Wang, M.X. Li, Mater. Sci. Eng. A 559 (2014) 247–254.
[38] L. Yu, Y.S. Geng, Q. Li, J.H. Wang, Z.Y. Liu, D.W. Li, in: Proceedings of the 55th Conference on Electrical Contacts, 2009, pp. 195–199.
[39] J. Wang, Y.Q. Kang, C. Wang, J.B. Wang, C. Fu, J. Alloys. Compd. 756 (2018) 202–207.
[40] Z.K. Chen, K. Sawa, J. Appl. Phys. 76 (1994) 3326–3331.
[41] J. Tepper, M. Seeger, T. Votteler, V. Behrens, T. Honig, IEEE Trans. Comp. Pack. Technol. 29 (2006) 658–665.
[42] P.G. Slade, The Vacuum Interrupter: Theory, Design, and Application, CRC Press, Taylor & Francis Group, Boca Raton, 2008, pp. 304–318.
[43] X.J. Liu, H.J. Fei, Trans. China Electrotech. Soc. 16 (2001) 81–84 (in Chinese).
[44] R.L. Boxman, S. Goldsmith, A. Greenwood, IEEE Trans. Plasma Sci. 25 (1998) 1174–1186.
[45] Z.K. Chen, K. Sawa, IEEE Trans. Compon. Pack. Manuf. Technol. 18 (1995) 409–416.